Journal of Alloys and Compounds 892 (2021) 162061

Contents lists available at ScienceDirect

Journal of Alloys and Compounds

journal homepage: www.elsevier.com/locate/jalcom

# A combined micro-Raman, X-ray absorption and magnetic study to follow the glycerol-assisted growth of epsilon-iron oxide sol-gel coatings

Jesús López-Sánchez[a,b,c,*], Aída Serrano[d], Adolfo del Campo[d], Álvaro Muñoz-Noval[a,b,c], Eduardo Salas-Colera[b,c,e], Mariona Cabero[f], María Varela[f], Manuel Abuín[g], Germán R. Castro[b,c], Juan Rubio-Zuazo[b,c], Óscar Rodríguez de la Fuente[a,h], Noemí Carmona[a,h]

[a] Departamento de Física de Materiales, Universidad Complutense de Madrid (UCM), 28040 Madrid, Spain
[b] SpLine, Spanish CRG BM25 Beamline, ESRF-The European Synchrotron, 38000 Grenoble, France
[c] Instituto de Ciencia de Materiales de Madrid (ICMM-CSIC), 28049 Madrid, Spain
[d] Instituto de Cerámica y Vidrio (ICV-CSIC), 28049 Madrid, Spain
[e] Departamento de Física, Escuela Politécnica Superior, Universidad Carlos III de Madrid, 28911 Leganés, Spain
[f] Instituto Pluridisciplinar & Departamento de Física de Materiales, Universidad Complutense de Madrid (UCM), 28040 Madrid, Spain
[g] Instituto de Sistemas Optoelectrónicos y Microtecnología (ISOM-UPM), 28040 Madrid, Spain
[h] Instituto de Magnetismo Aplicado (IMA-UCM-ADIF), 28230 Madrid, Spain

ARTICLE INFO

*Article history:*
Received 15 July 2021
Received in revised form 16 September 2021
Accepted 19 September 2021
Available online 30 September 2021

*Keywords:*
Epsilon iron oxide
Sol-gel Method
Glycerol as a steric agent
X-ray absorption spectroscopy
Confocal Raman microscopy
Magnetism

ABSTRACT

Epsilon iron oxide (ε-$Fe_2O_3$) coatings on Si(100) substrates are obtained by an easy one-pot sol-gel recipe assisted by glycerol in an acid medium. Glycerol, given its small dimensions, enables the formation of ε-$Fe_2O_3$ nanoparticles with a size of a few nanometers and the highest purity is reached in coatings after a densification treatment at 960 °C. The structural and compositional evolution up to 1200 °C is studied by confocal Raman microscopy and X-ray absorption spectroscopy techniques, correlating the existing magnetic properties. We report a novel characterization method, which allows monitoring the evolution of the precursor micelles as well as the intermediate and final phases formed. Furthermore, the inherent industrial technology transfer of the sol-gel process is also demonstrated with the ε-$Fe_2O_3$ polymorph, impelling its application in the coatings form.



## 1. Introduction

It is surprising to observe the increasing capabilities over time of epsilon iron oxide (ε-$Fe_2O_3$) to exhibit multiple functionalities. The synthesis of this elusive iron oxide polymorph was mastered relatively recently, and it was obtained in pure form by inexpensive, widespread sol-gel methods in 2004 [1,2]. To date, considerable efforts have been undertaken to synthesize it in pure form not only by sol-gel synthesis [3–10], but also by pulsed laser deposition (PLD) [11–14] and atomic layer deposition (ALD) [15]. However, it exists mainly confined to the nanoscale due to its high bulk energy [16] and complex crystalline structure (orthorhombic crystal structure with the $Pna2_1$ space group and lattice parameters a=5.095 Å, b=8.789 Å, and c=9.437 Å [17]). ε-$Fe_2O_3$ displays interesting physical properties that are of great relevance in basic science [9,18–23] and, more recently, also in technology [24]. Epitaxial films exhibit multiferroic properties at room temperature [11], while nanoparticles show a high efficiency in magnetic hyperthermia [25], ultrafast Faraday rotation effects under terahertz pulsed light [26], and microwave absorption in the terahertz range [27,28]. ε-$Fe_2O_3$ nanoparticles are also palaeointensity markers in baked clay archaeomagnetic materials [29,30], and they present excellent capabilities for flexible high-density recording media [31].

During the synthesis process of ε-$Fe_2O_3$, the thermodynamic conditions favor the most stable phase of iron oxide, i.e. the hematite phase (α-$Fe_2O_3$), due to a larger size of the precursor micelle [16,32]. As a consequence, the densification thermal range of ε-$Fe_2O_3$ formation is relatively narrow [6,33]. Therefore, a short carbon chain polyalcohol rich in hydroxyl groups, such as glycerol (GLY), is a suitable candidate to enclose the precursor micelle into a silica matrix with the smallest possible dimensions and thus create both continuous and homogeneous coatings [34,35]. Under these premises, a reproducible sol-gel recipe assisted by GLY is proposed in this work to obtain

* Corresponding author at: Departamento de Física de Materiales, Universidad Complutense de Madrid (UCM), 28040 Madrid, Spain.
*E-mail address:* jesus.lopez@ucm.es (J. López-Sánchez).

https://doi.org/10.1016/j.jallcom.2021.162061
0925-8388/

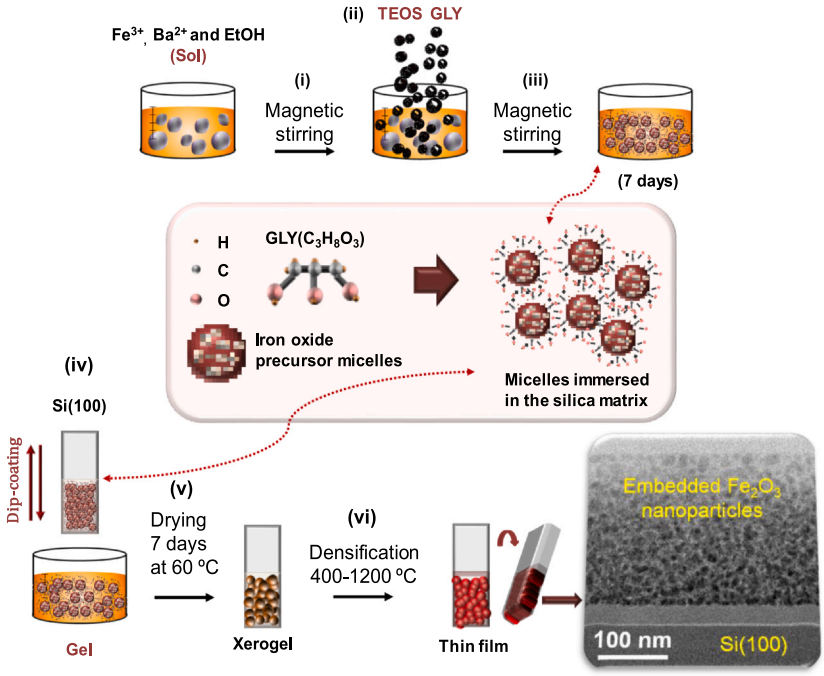


**Fig. 1.** GLY-based sol-gel synthesis in an acidic media of continuous and homogeneous mesoporous silica films containing iron oxide-based compounds. (i) Firstly, iron and barium nitrates are added to form the primary micelles in an alcoholic solution where they are magnetically stirred at vigorous speed and the hydrolysis-polycondensation processes start. (ii) Subsequently, TEOS and GLY are added dropwise, and (iii) the resulting solution is kept magnetically stirred for 7 days at room temperature. (iv) The resulting gel is deposited on commercial Si(100) substrates at a constant speed by a dip-coating process. (v) The coatings are dried for 7 days at 60 °C to evaporate the alcoholic groups formed. (vi) The densification treatment is carried out at 400–1200 °C in an air atmosphere. As an example, a cross-sectional scanning transmission electron microscopy (STEM) image related to a sample treated at 960 °C is added (bottom right).

coatings composed of ε-$Fe_2O_3$ nanoparticles embedded in a silica matrix on Si(100) substrates. The synthetic route is designed to understand the different stages of the iron oxide precursor micelle from its first steps forming iron oxyhydroxides to obtaining the ε-$Fe_2O_3$ polymorph. In the proposed scenario, the evolution of the compounds formed during the densification process is investigated from the removal of the organic compounds (T ~ 400 °C), to the formation of ε-$Fe_2O_3$ (900 ºC < T < 1200 ºC), and the gradually transformation into α-$Fe_2O_3$ at the highest temperatures. This kind of structural studies has been carried out by Mössbauer spectroscopy and X-ray diffraction (XRD) [2,10,21,36]. The aim of this work is to provide an alternative and novel advanced characterization using confocal Raman microscopy (CRM) and X-ray absorption spectroscopy (XAS) techniques, correlating them with the magnetic properties exhibited.

The results obtained in this research establish the thermal constraints for obtaining an oxyhydroxide (ferrihydrite, FH) and iron oxides (γ-, ε-, and α-$Fe_2O_3$), where the ε-$Fe_2O_3$ polymorph stands out for its potential multifunctionality. On the one hand, the designed sol-gel synthesis represents a substantial advance in the growth of iron oxide phases and, specifically, the fabrication of ε-$Fe_2O_3$ polymorph films by the sol-gel method. On the other hand, the novel structural characterization of the evolution of the compounds by CRM and XAS techniques enables the temperature-dependent compositional optimization to improve the response of the ε-$Fe_2O_3$ polymorph in technological applications of immense relevance such as high-density magnetic recording media or microwave absorption in the terahertz range [27,28,31].

## 2. Material synthesis and experimental methods

### 2.1. GLY-based sol-gel synthesis to obtain iron(III) oxide nanoparticles

An illustration of the entire glycerol-based sol–gel synthesis is shown in Fig. 1. The synthesis is carried out starting from a solution of absolute ethanol ($CH_3CH_2OH$, Panreac), acting as solvent for the salts of iron nitrate nonahydrate ($Fe(NO_3)_3.9H_2O$, Sigma-Aldrich > 98%) and barium nitrate ($Ba(NO_3)_2$, Sigma-Aldrich > 98%), with a molar ratio of 1:0.002 respectively. The pH of the sol is close to unity, favoring the hydrolysis and polycondensation processes of the iron oxide precursor micelles in an acid media (Fig. 1i). Subsequently, the chemical reactions of the formation of the silica matrix occur simultaneously with a dropwise addition of the silica matrix precursor, tetraethyl orthosilicate (TEOS, $SiC_8H_{20}O_4$, Sigma-Aldrich > 98%), with an Fe:Si molar ratio of 1:1. Once a homogeneous solution is achieved, GLY ($C_3H_8O_3$, Sigma-Aldrich > 99%) is slowly added drop by drop with a molar ratio to TEOS of (1.5:1, respectively) (Fig. 1ii). The slow dropwise addition of the TEOS and GLY precursors is essential to facilitate the homogenization of the sol, i.e. the optimal and equal formation of the iron oxide precursor micelles and the silicic acids formed after the first hydrolysis and polycondensation steps. In addition, the GLY hydroxyl groups promote the hydrolysis processes and the viscosity of the resulting solution is notably increased.

All the stages are supported by the presence of nitric acid ($HNO_3$, Sigma-Aldrich > 70%), which acts as a catalyst for the chemical reactions at room temperature. The obtained solution is kept magnetically stirred for 7 days under a vigorous speed at room temperature to enhance the particle size distribution and purity of the resulting samples (Fig. 1iii) [9,21]. Afterwards, sol-gel coatings are deposited on Si(100) wafers (as received) by a dip-coating process (Fig. 1iv) and they are dried in a conventional oven at 60 °C for 7 days in order to remove the excess of alcoholic groups formed (xerogel formation, Fig. 1v). Finally, the densification of the coatings is performed by thermal treatments between 400 and 1200 °C in an air environment with a heating rate of 1 °C/min (Fig. 1vi). The final films are composed of 54 wt% of iron oxide-based products in a silica matrix. The coatings display final thicknesses of ~760 nm and ~200 nm, which are adjusted by the dip-coating speed 4.52 and 2.56 mm/s, respectively (see atomic force microscopy (AFM) images in the Supporting Information).

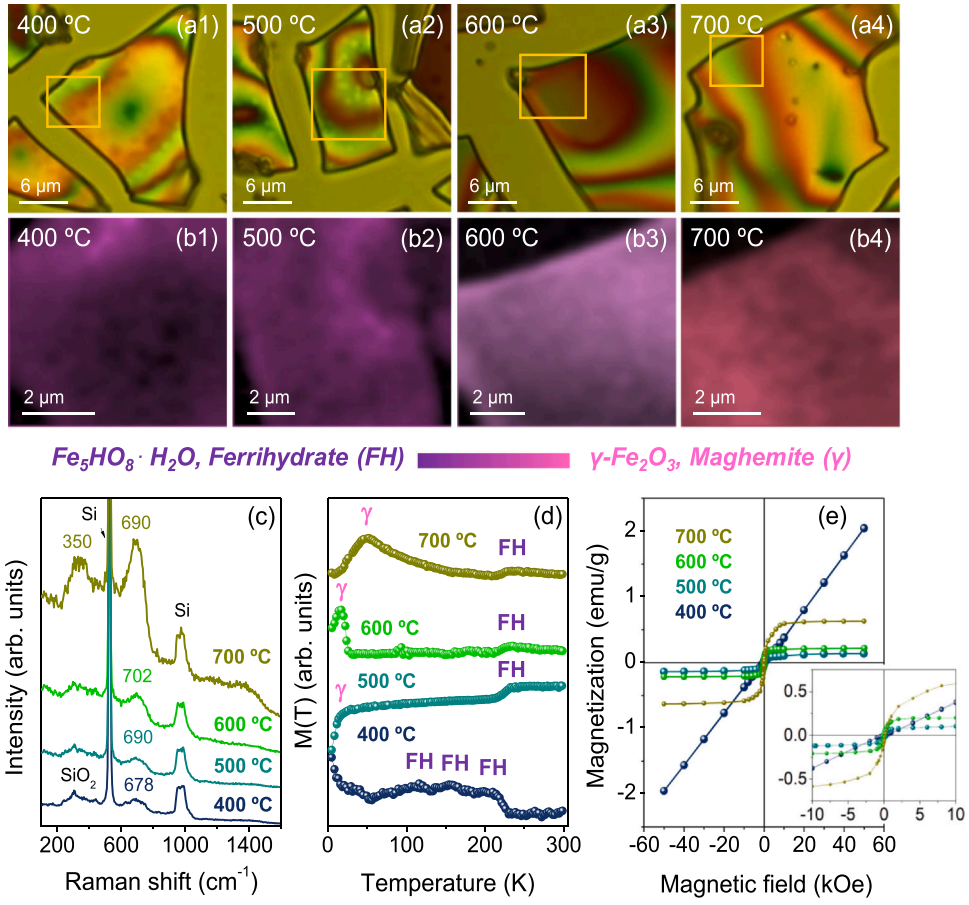


**Fig. 2.** Micro-Raman study and magnetic properties of samples prepared at 400, 500, 600, and 700 °C. (a1–4) Optical micrographs. (b1–4) Raman intensity images in the XY plane corresponding to the yellow boxes in Fig. a1–4. The integration range chosen for intensity mappings goes from 660 to 750 $cm^{-1}$. (c) Average Raman spectra obtained from the Raman intensity images (Fig. b1–4). (d) M(T) curves taken from 5 to 300 K. (e) Magnetic hysteresis loops collected at 300 K where the diamagnetic effect of the Si substrate has been corrected. The inset in Figure e represents a magnification of the central area for clarity.

### *2.2. Structural and magnetic characterization*

Compositional and structural properties are investigated using a Witec ALPHA 300RA confocal Raman microscope equipped with a Nd:YAG laser (532 nm in p-polarization) and by XAS experiments carried out at the Spanish CRG beamline BM25-SpLine at The European Synchrotron (ESRF), Grenoble (France). From Raman measurements, intensity mappings of representative areas are performed in densified samples with a 100x objective lens (numerical aperture of 0.95), in which Raman spectra are acquired every 200 nm with 5 s of integration time. The laser power employed is fixed at 0.7 mW to avoid overheating effects. The Raman intensity is proportional to the amount of material and the characteristics of the Raman bands are related to parameters such as the degree of crystallinity and/or the dimensions [37]. In this sense, in order to obtain the best quality of Raman signal, it is determined that the coatings prepared between 400 and 900 °C have an optimal thickness close to ~760 nm. On the contrary, for the samples treated from 960 to 1200 °C, coatings of ~200 nm are considered suitable for the Raman compositional study. Optical images and complementary AFM images are recorded by the same equipment with a gold-coated silicon probe, NSG30 model provided by NT-MDT (Russia). The tip is about 14–16 µm high, aspect ratio from 3:1–5:1 and a radius of 10 nm. The cantilever is 125 µm long, 40 µm wide and 4 µm thick, with an elastic constant 40 N/m and a resonant frequency of ~268 kHz. Raman and AFM data are analyzed using the Witec Project Plus software. Regarding the XAS measurements, both X-ray absorption near edge structure (XANES) and extended X-ray absorption fine structure (EXAFS) regions are analyzed at the Fe K-edge (7112 eV) in fluorescence yield mode in the range between 6900 and 8000 eV. Signals are collected using a 13 element Si(Li) solid state detector (INCA, Sgx Sensortech). XAS spectra are analyzed according to standard procedures using the ATHENA program package [38].

Morphological features and nanoparticle distribution into the film are examined by cross sectional scanning transmission electron microscopy (STEM) images with a JEOL ARM 200cF STEM, working with a CEOS aberration corrector under a cold field emission source operated at 200 kV. Simultaneous electron energy-loss spectroscopy (EELS) measurements are obtained in selected areas to study the chemical composition along with the formal oxidation states of the nanoparticles.

The magnetic properties of the coatings are evaluated with a quantum design MPMS-XL magnetometer. Hysteresis magnetic loops are obtained at room temperature with a maximum applied magnetic field of 50 kOe. Temperature dependence curves (M(T)) are collected in the temperature range from 5 to 300 K at 200 Oe.

## 3. Results and discussion

### *3.1. A combined vibrational and magnetic study*

Fig. 2a1–4 show the optical micrographs corresponding to the samples prepared between 400 and 700 ºC. In them, cracks produced during the densification process might arise due to the increase of the surface energy of the coating and/or to differences in the coefficients of thermal expansion between substrate and coating. In turn,

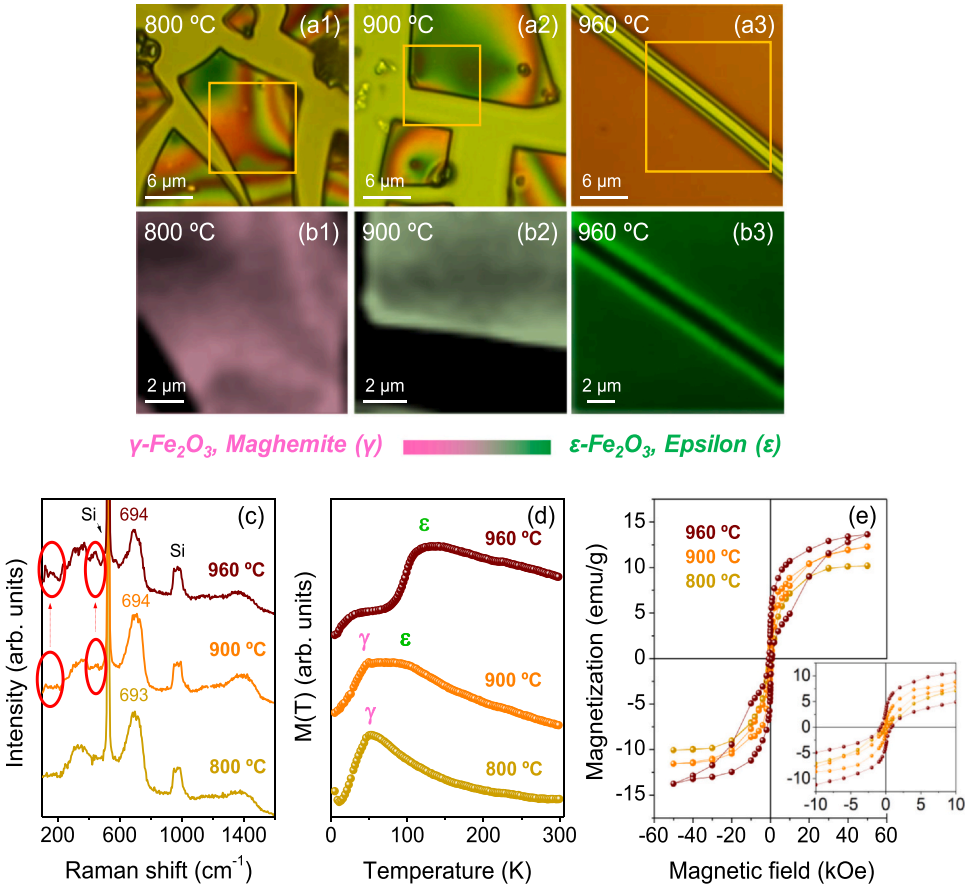


**Fig. 3.** Micro-Raman study and magnetic properties of samples prepared at 800, 900, and 960 ºC. (a1–3) Optical micrographs. (b1–3) Raman intensity mappings in the XY plane corresponding to the yellow boxes on optical images in Fig. a1–3. The integration range chosen for intensity imaging goes from 660 to 750 $cm^{-1}$ for γ-$Fe_2O_3$ (pink color) and from 100 to 200 $cm^{-1}$ for ε-$Fe_2O_3$ phase (green color). (c) Average Raman spectra obtained from the Raman intensity images (Fig. b1–4). Red ellipses indicate the emerging of the ε-$Fe_2O_3$ phase. (d) M(T) curves taken from 5 to 300 K. (e) Magnetic hysteresis loops collected at 300 K where the diamagnetic effect of the Si substrate has been corrected. The inset of Figure e represents a magnification of the central area for clarity.

the coating is transparent and colored stripes are visible as a result of optical interferences. Several CRM scans are performed in the XY plane in different zones to identify the composition of the samples as well as their degree of homogeneity. Representative regions in each sample are displayed as yellow rectangle areas in Fig. 2a1-a4. Raman intensity images, shown in Fig. 2b1–4, are calculated by integrating the band around 700 $cm^{-1}$, which evolves with temperature and could be related to the presence of an iron oxide-based compound [39]. The average Raman spectra from the corresponding Raman mappings are represented in Fig. 2c. The characteristic Raman modes of the Si substrate are observed in all the spectra and they are localized at 304, 512, and 970 $cm^{-1}$ [40]. The integrated Raman mode at 700 $cm^{-1}$ might attribute to several oxyhydroxides and iron oxide phases such as FH, γ-$Fe_2O_3$, and ε-$Fe_2O_3$ [23,41,42]. Therefore, an assignation of compositional phases presented in the samples is not possible at a glance. To elucidate the nature of the iron-based compounds formed with the densification temperature, M(T) curves are performed to detect possible magnetic transitions that can be associated with the main phase present in the coating (Fig. 2d).

For the sample densified at 400 °C, a broad bump is found ranging from ~50 to ~220 K with three main shoulders located at ~115, ~159, and ~210 K (Fig. 2d). The origin of those shoulders is probably due to the characteristic blocking temperatures related to the FH phase with different particle sizes [43,44]. FH is the most common precursor of other iron oxides and hydroxides, both synthetically and naturally produced [45]. Its sizes are typically comprised between 2 and 7 nm [46] and it behaves as an antiferromagnetic material with a Néel temperature of ~240 K above ~8 nm [47]. It has a high surface area that provides a high chemical reactivity [48]. Interestingly, slight differences in particle size drastically change its magnetic properties [43]. While 2-line FH (~2–4 nm) usually displays a blocking temperature of ~50 K [46,49,50], 6-line FH (~6–7 nm) exhibits blocking temperatures up to 200 K [44]. Considering this, M(T) curves show how the FH particle size evolves towards its bulk behavior with a Néel temperature of ~240 K (Fig. 2d) at 500, 600, and slightly at 700 °C.

Fig. 2e shows the hysteresis loops of the samples prepared from 400 to 700 °C. At 400 °C, a paramagnetic response is observed. However, the superparamagnetic hysteresis loops observed at 500, 600, and 700 °C are not attributed to FH, which is paramagnetic at room temperature. Commonly, FH immersed in a silica matrix transforms into maghemite (γ-$Fe_2O_3$) as temperature increases [16]. Specifically to this work, γ-$Fe_2O_3$ displays a superparamagnetic character at room temperature (Fig. 2d) and its blocking temperatures are clearly detected at ~16 K for 600 °C and at ~50 K for 700 °C, together the Néel temperature of FH in the samples densified between 500 and 700 °C at 240 K (Fig. 2d). In addition, as the FH transforms into γ-$Fe_2O_3$, the saturation magnetization gradually increases with temperature up to 700 °C because its higher saturation value [45] (Fig. 2e). To determine the average particle sizes corresponding to those blocking temperatures, calculations are performed according to the Néel-Arrhenius relation [51]:

$$\tau_N = \tau_0 e^{K \ V/k_B \ T} \quad (1)$$

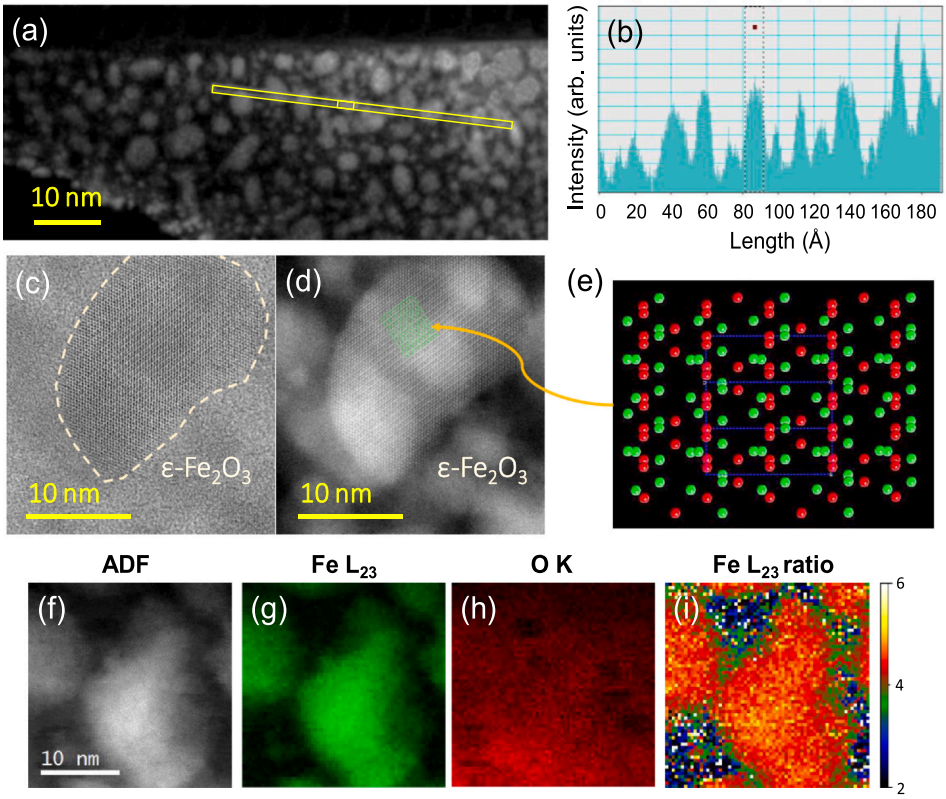


**Fig. 4.** Structural characterization of sample densified at 960 ºC. (a) HAADF image. (b) Intensity profile of the nanoparticles, which shows the approximate size of the nanoparticles to be around 7–15 nm. Simultaneously acquired (c) ABF and (d) HAADF images from the same ε-$Fe_2O_3$ nanoparticle oriented in the [210] direction. (e) Illustration of the ε-$Fe_2O_3$ crystal structure, exhibiting both the Fe atoms (green) and O atoms (red) down the [210] direction; (f) ADF image of another nanoparticle where an EEL spectrum image was acquired to produce the adjacent (g) Fe $L_{23}$ and (h) O *K* edge maps (in false color). (i) Fe $L_{23}$ ratio map for the same particle. The value corresponding to iron (III) oxide is 4.5 [56].

where $\tau_N$ is the average time of the magnetization reversal due to thermal fluctuations; $\tau_0$ is the characteristic attempt time of the material, whose value ranges from $10^{-9}$ or $10^{-12}$ s; $k_B$ is the Boltzmann constant, K is the magnetic anisotropy constant, and V is the particle volume. Taking the $K_{Maghemite}$ value of $10^5$ J $m^{-3}$ [45] and, considering this value as constant even if the particle dimensions are slightly varied, average particle sizes of ~2.4 nm for ~16 K and ~3.5 nm for ~50 K are obtained (Table S1 in the Supporting Information).

Summarizing, with these magnetic results, the Raman band located around 700 $cm^{-1}$ of the samples prepared between 400 and 600 ºC might be mainly attributed to FH (Fig. 2c), although the γ-$Fe_2O_3$ phase could be contributing to that Raman signal. The sample synthesized at 600 ºC is included since no significant deviation in the Raman position is detected as the temperature increases. However, a band narrowing is observed and this effect might be related to an increase of the crystallinity degree and/or particle size [23] of FH nanoparticles. A larger γ-$Fe_2O_3$ fraction might also be considered. In contrast, for the case of 700 ºC, two of the three characteristic bands of the nanometric γ-$Fe_2O_3$ are distinguished (350 and 690 $cm^{-1}$ [42]), identifying the γ-$Fe_2O_3$ as the main iron oxide phase present.

Similarly, the densification range of coatings between 800 and 960 °C is analyzed. The optical micrographs of the samples treated at 800 and 900 °C (Fig. 3a1–2) show strong similarities with respect to those shown in Fig. 2a1–4. From 960 ºC, the decrease of the coating thickness seems to improve its continuity and homogeneity on the substrate surface (Fig. 3a3). This effect could be due to the evaporation process of the alcoholic groups formed during the sol-gel process, which are released easier for lower thicknesses, producing less cracks. The calculated XY-plane Raman intensity images are presented in Fig. 3b1–3 and the obtained average Raman spectra are displayed in Fig. 3c. In them, a higher Raman intensity of the iron oxide phases and a narrowing of their Raman bands are identified, and an assignation of the phases is easier. The Raman spectrum of the sample treated at 800 °C corresponds to γ-$Fe_2O_3$ with particles of nanometer size [42]. From 900 °C onwards, the characteristic Raman spectrum of the ε-$Fe_2O_3$ polymorph begins to be defined with the emergence of new Raman modes, clearly visible in the spectral ranges 100–200 $cm^{-1}$ and 450–500 $cm^{-1}$ (indicated by red ellipses in Fig. 3c) [33].

M(T) curves corresponding to the synthesis temperatures of 800, 900, and 960 °C are shown in Fig. 3d. At 800 ºC, the characteristic blocking temperature of γ-$Fe_2O_3$ is detected at around 50 K [52]. However, this transition is accompanied by the occurrence of another contribution at 100 K for the 900 ºC sample (Fig. 3d). In that temperature range the incommensurate magnetic transition of ε-$Fe_2O_3$ is located [21,53]. Therefore, a phase coexistence is observed and the Raman spectrum must correspond to the mixture of both polymorphs, i.e. γ-$Fe_2O_3$ and ε-$Fe_2O_3$ (Fig. 3c-d). In contrast, going to the 960 ºC sample, a well-defined incommensurate magnetic transition of the ε-$Fe_2O_3$ polymorph around ~100 K is discerned [21,53]. A small shoulder around ~25 K is visible (Fig. 3d), which might be due to α-$Fe_2O_3$ nanoparticles with a size of ~5 nm [7]. This contribution can be considered as minority since hematite is not detected by CRM measurements, in spite of its high scattering power [54]. Interestingly, no superparamagnetic transition attributed to γ-$Fe_2O_3$ is found. Therefore, it is proposed that γ-$Fe_2O_3$ is not present using a densification temperature above 960 ºC. The hysteresis loop of the sample synthesized at 800 ºC (Fig. 3e) shows the same superparamagnetic characteristics as in the 700 ºC sample (Fig. 2e), except for a remarkable increase in the saturation magnetization

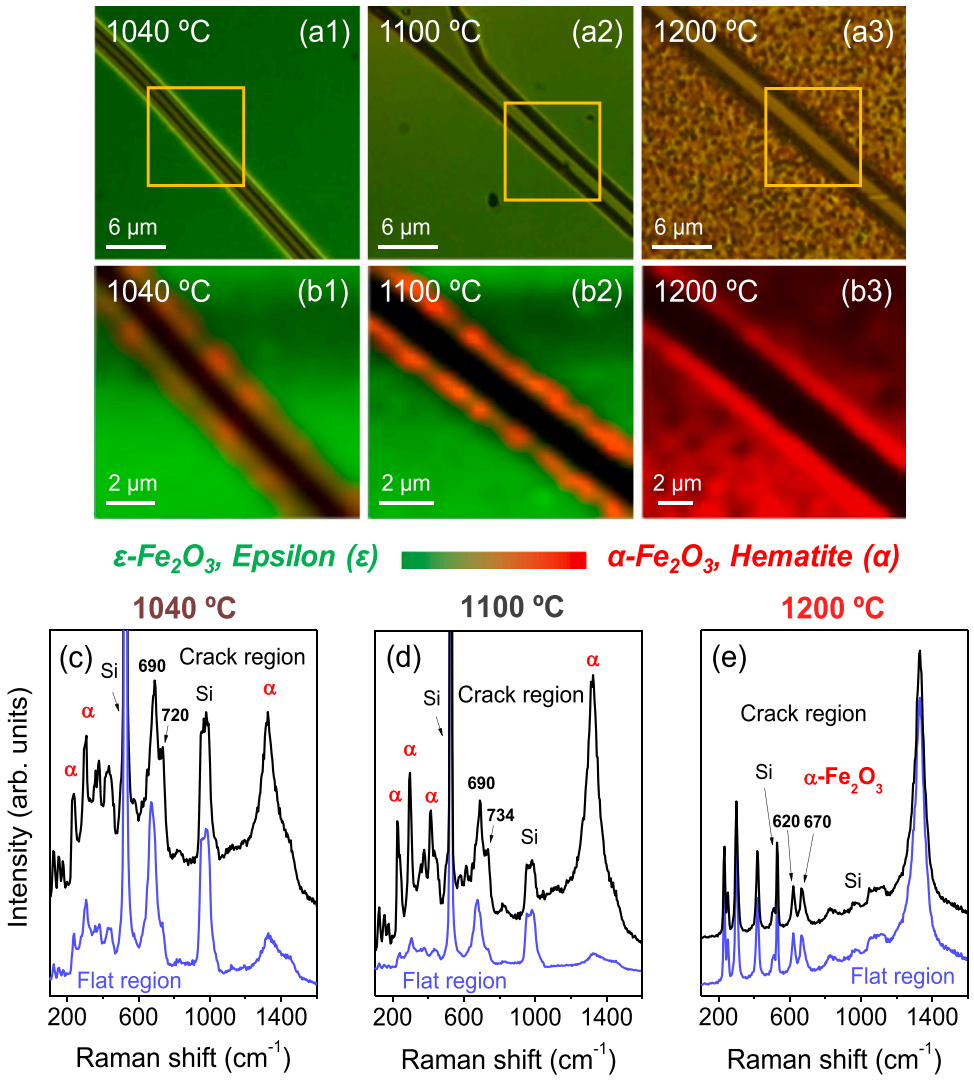


**Fig. 5.** Micro-Raman study of samples prepared at 1040, 1100, and 1200 ºC. (a1–3) Optical micrographs. (b1–3) Raman intensity images in the XY plane obtained from the yellow boxes in Fig. a1–3. The integration range chosen for intensity imaging goes from 100 to 200 $cm^{-1}$ for ε-$Fe_2O_3$ (green), and from 1310 to 1350 $cm^{-1}$ for α-$Fe_2O_3$ (red). (c-e) Average Raman spectra obtained from the crack and flat regions identified in Fig. b1–3 for the corresponding samples.

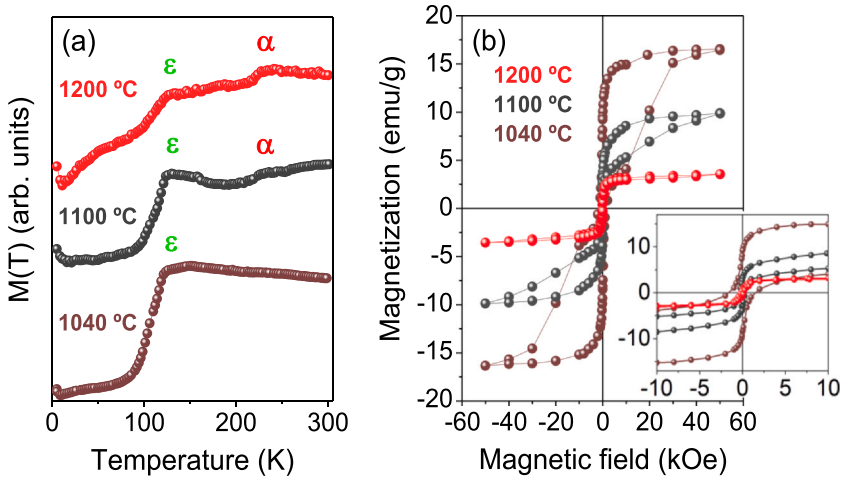


**Fig. 6.** (a) M(T) curves in the range 5–300 K and (b) magnetic hysteresis loops collected at 300 K for the samples densified at 1040, 1100, and 1200 ºC. The diamagnetic contribution of the Si substrate is corrected. The inset of Fig. b shows a magnification of the central area for inspection.

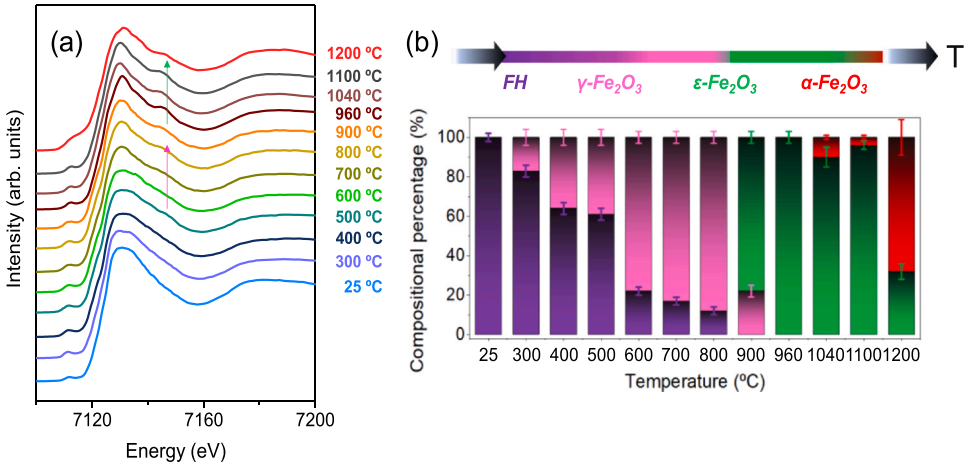


**Fig. 7.** (a) XANES spectra collected from coatings prepared from 25 to 1200 ºC. The pink and green arrows indicate the emergence of a well-defined second resonance corresponding to the notable appearance compositional phases present in each sample. (b) Diagram of compositional evolution with the densification temperature calculated from a linear combination fitting taking into account a FH, α-$Fe_2O_3$, γ-$Fe_2O_3$, and ε-$Fe_2O_3$ references.

from ~0.5 to ~6 emu/g. The inset in Fig. 3e reveals that the hysteresis loop begins to broaden and the coercivity increases above 900 ºC. These results are evidences of the formation of ε-$Fe_2O_3$ and typical saturation magnetization values are present for sample at 960 ºC, comparing to other works [5,21]. Similarly, the coercivity grows with the particle size and it attains ~20 kOe for d > 30 nm [6].

To correlate the structural and magnetic properties obtained for the 960 ºC sample, cross-section high resolution STEM measurements are performed (Fig. 4). The particle size along the coating is examined by high angle annular dark field (HAADF) images. Fig. 4a displays results from a sample with a high density of nanoparticles embedded in a silica matrix. Fig. 4b shows the intensity profile measured along the area highlighted with a yellow rectangle in Fig. 4a. The particle diameters observed range from 7 to 15 nm. Accordingly, the synthesized ε-$Fe_2O_3$ nanoparticles have a reduced coercivity and the hysteresis loop exhibited in Fig. 3e is justified. As an example, annular bright field (ABF) and HAADF images acquired in the same ε-$Fe_2O_3$ nanoparticle are shown in Fig. 4c-d. The nanoparticle is orientated along the [210] direction and the simulated crystal structure is superimposed on the HAADF image (Fig. 4e, Fe atoms in green, O in red), displaying the Fe atoms (O atoms are removed for the sake of clarity).

In addition, we have performed in the same instrument electron energy-loss spectroscopy (EELS). An EELS spectrum image provides information about the formal oxidation state of the iron oxide nanoparticle under study. The $L_2$ and $L_3$ absorption edges (white-lines) of Fe arise from the excitation of the core electrons found in the $2p_{1/2}$ and $2p_{3/2}$ orbitals to the unoccupied electronic states of the *d* orbitals near the Fermi level (dipole transitions) and the intensities of the absorption edges represent the density of states of the unoccupied *3d* orbitals [55]. Subsequently, an in-situ intensity scan is performed specifically in a nanoparticle (Fig. 4f), obtaining the signature of the $L_3$ and $L_2$ absorption edges of Fe (Fig. 4g) and the *K* edge of O (Fig. 4h). The intensity ratio between lines $L_3/L_2$, also known as $L_{23}$ ratio, shows a value of ~4.5 (Fig. 4i), which corresponds to Fe 3 + oxidation state [56]. From the present findings, a good degree of homogeneity in the nanoparticle is deduced, which is consistent with an iron (III) oxide. Its formal oxidation state is only slightly reduced at its boundaries, which are in close contact with the silica matrix. The same analysis is performed for different nanoparticles obtaining similar results.

In the last densification temperature range from 1040 to 1200 ºC, the transformation of ε-$Fe_2O_3$ to α-$Fe_2O_3$ is gradually reached with temperature. The morphology of the coatings is reflected in the optical micrographs in Fig. 5a1–3. From the Raman microscans of the sample prepared at 1040 °C (Fig. 5b1), two distinct Raman spectra are distinguished (Fig. 5c). One spectrum is collected at the crack boundary region (with more amount of material, see Supporting Information) and the other one is collected from the flat region. Both of them show characteristics of the Raman spectrum of ε-$Fe_2O_3$ and α-$Fe_2O_3$ (they are intermixed), but the intensity ratios of their Raman modes are different due to the change of their compositional fraction. The flat region contains less α-$Fe_2O_3$ and the bands between 640 and 750 $cm^{-1}$ are enhanced in intensity and shifted towards lower Raman frequencies compared to those bands in the Raman spectrum associated with the crack boundary region (Fig. 5c). The bands appear sharper compared to the lower densification samples and it is probably caused by the formation of larger particle sizes [23].

In the 1100 ºC sample, similar structural properties are found, but some differences are observed with respect to the previous sample (Fig. 5c-d). The amount of ε-$Fe_2O_3$ in the flat region is still remarkable (Fig. 5b2,d). However, α-$Fe_2O_3$ becomes the predominant phase in the crack boundary region since its Raman intensity is highly enhanced (Fig. 5d). Moreover, the Raman bands are narrower as a sign that the particle size is increased [23,37]. At 1200 °C, the morphological and structural changes of the coating are visible in the optical micrograph in Fig. 5a3. Nanostructured particles can be discerned in the flat region, resulting in an increase of the surface roughness. Interestingly, the ε-$Fe_2O_3$ polymorph is not detected in the areas studied along the present coating. Here, α-$Fe_2O_3$ is the predominant compound and no appreciable structural differences are detected in the average Raman spectra acquired in the flat and crack boundary regions (Fig. 5b3,e). Accordingly, the thermal threshold is fixed where the ε-$Fe_2O_3$ polymorph might be fully transformed into α-$Fe_2O_3$ according to CRM measurements.

In the M(T) curves, the incommensurate magnetic transition of the ε-$Fe_2O_3$ polymorph is detected around 115–120 K for both 1040 and 1100 ºC samples (Fig. 6a) [5]. In addition, a small shoulder exists around ~240 K that could be related to the Morin transition of α-$Fe_2O_3$ at 1100 ºC [45]. This transition might correspond to α-$Fe_2O_3$ agglomerates or larger particles that behave like a larger particle size one, when they are placed in close contact with a ferromagnetic material [57,58]. At 1200 ºC, the magnetization gradually increases with temperature and no clear magnetic transitions are indexed excepting the Morin transition at 240 K and a small singularity around 120 K attributable to the ε-$Fe_2O_3$ polymorph (Fig. 6a). However, considering the predominance of the α-$Fe_2O_3$ observed from the Raman results (Fig. 5e), the contribution of the ε-$Fe_2O_3$ polymorph is considered minority at 1200 ºC.

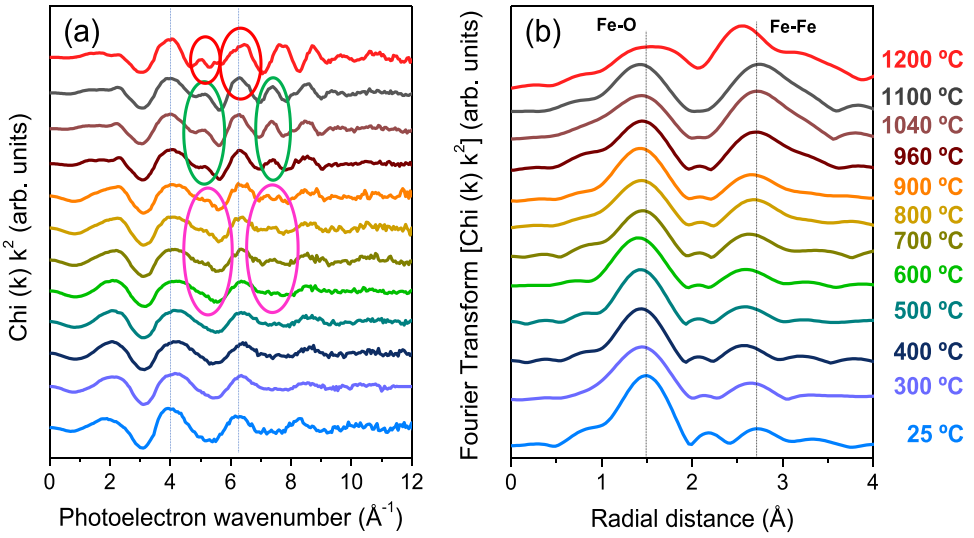


**Fig. 8.** (a) k$^2$-weighted EXAFS-$\chi$(k) spectra of the coatings prepared from 25 to 1200 ºC. The pink, green, and red ellipses indicate structural variations arising from the emergence of new phases ($\gamma$-$Fe_2O_3$, $\varepsilon$-$Fe_2O_3$, and $\alpha$-$Fe_2O_3$, respectively). Vertical visual guides are added for proper inspection. (b) Fourier transform of the EXAFS-$\chi$(k) spectra represented in R-space. The shells corresponding to the interatomic distances related to Fe–O and Fe–Fe atoms are signaled with vertical guides.

Fig. 6b represents the magnetic hysteresis loops corresponding to the samples treated at 1040, 1100, and 1200 ºC. The hysteresis loop widens, the coercivity increases, and the saturation magnetization (50 kOe) is not achieved at 1040 and 1100 ºC. In this sense, the saturation magnetization reaches the highest value at 1040 ºC (~16 emu/g) and the low-coercivity magnetic contribution is significantly reduced compared to the rest of the samples. In contrast, the saturation magnetization diminishes up to ~9 emu/g at 1100 ºC. This might be due to the highest $\alpha$-$Fe_2O_3$ content found in Fig. 5b2 and d. In turn, the hard contribution of the $\varepsilon$-$Fe_2O_3$ polymorph is vanished at 1200 ºC and a notable reduction of the magnetic response is noticed.

### 3.2. A combined structural short-range order and magnetic study

The XANES spectra presented in Fig. 7a illustrate the compositional evolution throughout the densification treatment of samples up to 1200 ºC, identifying subtle differences between them. For the untreated sample, a pre-peak around 7111 eV is identified, which is associated with the 1 s → 3d quadrupole transition and 1 s → 3d/4p dipole transition [59] and remains present at all the densification temperatures. However, a drastic change is noted in the shape of the pre-peak at 1200 ºC suggesting a chemical change in the sample that might be related to some reaction with the substrate. At lower densification temperatures, the XANES spectra exhibit relatively wide whitelines that are accompanied by broad resonances, which can be explained by the nature of nanometer particles with reduced crystalline order in this temperature range [60]. For the sample prepared at 600 ºC and above, the whiteline after the absorption edge narrows and the intensity related to the second resonance arises (indicated by a pink arrow in Fig. 7). As the synthesis temperature increases, the whiteline continues to narrow and a shoulder at lower energies is observed, showing the typical characteristics of the $\varepsilon$-$Fe_2O_3$ polymorph (marked with a green arrow in the Fig. 7) [9]. From 960 ºC the XANES signal continues to evolve up to 1200 ºC, where the characteristic double peak of $\alpha$-$Fe_2O_3$ can be seen, proving that the $\alpha$-$Fe_2O_3$ is the prevailing phase at the highest temperature, i.e. 1200 ºC [9]. In addition, a major number of oscillations are noted, related to a large crystalline order in the $\alpha$-$Fe_2O_3$ structure.

In order to semi-quantify the compositional evolution with the densification temperature and correlate the results with the micro-Raman experiments, an estimation is calculated for each sample by a linear combination fitting of the first derivative of the XANES spectra from those of the FH, $\alpha$-$Fe_2O_3$, $\gamma$-$Fe_2O_3$, and $\varepsilon$-$Fe_2O_3$ references [9,21], as Fig. 7b shows. Initially for the untreated sample, a 100(2)% of FH is obtained, indicating that this phase is the precursor for the synthesis process of other iron oxides. From 300 ºC, the percentage of the FH gradually decrease up to 12(2)% for sample treated at 800 ºC and it

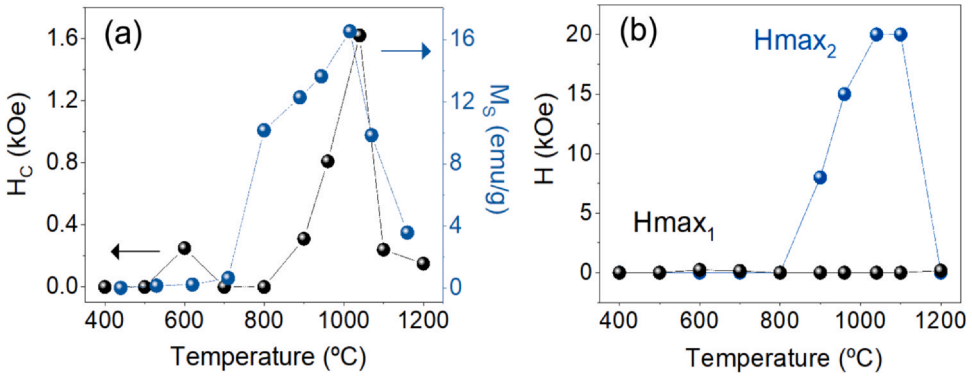


**Fig. 9.** (a) Coercivity ($H_C$, left side) and saturation magnetization ($M_S$, right side) of all the samples densified from 400 ºC to 1200 ºC. (b) Coercivities (Hmax$_{1,2}$) obtained from the derivative of the magnetic hysteresis loops for samples annealed in the range 400–1200 ºC.

disappears at higher temperatures. This compositional transformation is accompanied by the formation of γ-$Fe_2O_3$, which has an opposite trend with an increase from 17(4)% to 88(3)% from the 300 ºC to 800 ºC sample. At 900 ºC, its contribution suddenly decreases to 22(3)% and the majority presence of the ε-$Fe_2O_3$ phase appears, persisting up to 1100 ºC with a purity of 96(4)%. A 100(3)% of ε-$Fe_2O_3$ is obtained for sample annealed at 960 ºC. The ε-$Fe_2O_3$ contribution decreases significantly to 32(4)% for the sample annealed at 1200 ºC, and the rest compound corresponds to α-$Fe_2O_3$. Noteworthy is that these results corroborate the absorption characteristics noted in the XANES signal and the results previously described by Raman and magnetic properties.

The $k^2$-weighted EXAFS-$\chi$(k) spectra of the coatings prepared at different temperatures are shown in Fig. 8a. The spectrum related to the untreated 25 ºC sample exhibits structural changes with shifts towards higher wavenumbers compared to the sample treated at 300 ºC. This effect is probably due to the presence of organic groups bound to the ferric cations [61]. In the 400–600 ºC range, the organic groups are removed and no substantial structural deviations compared to 300 ºC are detected. Between 700 and 900 ºC, a contribution to the oscillatory signal (indicated by pink ellipses) arises that can be related to the large amount of γ-$Fe_2O_3$ identified by CRM analysis and XANES (Figs. 2 and 7, respectively). From 900 ºC onwards, new oscillations induced structures are defined (marked with green ellipses in Fig. 7) that increase in amplitude and progress up to 1100 ºC. In this range, ε-$Fe_2O_3$ is present with a considerable percentage (see Fig. 7b). Therefore, those new oscillations structures can be attributed to the ε-$Fe_2O_3$ polymorph [21]. Related to 1200 ºC, the $k^2$-weighted EXAFS-$\chi$(k) oscillating spectrum is significantly different from the previous ones (main variations indicated by red ellipses), and it is indicative of the dominant presence of hematite at 1200 ºC as previously has been identified by CRM (Fig. 5) and XANES (Fig. 7) experiments.

Fourier analyses are performed in the $k^2$ $\chi$(k)-weighted EXAFS oscillating signal between 2.5 and 11 $Å^{-1}$ and it provides information about the local structure in the R-space [62] as a function of the temperature (Fig. 8b). The untreated 25 ºC sample exhibits a main shell around ~2 Å with a pronounced intensity and it may be mainly related to Fe–O interatomic distances [9]. Its relatively broad could attribute to the presence of other Fe chemical environments (different speciation) and/or a large static disorder [61]. In addition, the absence of a second shell may explain the lack of crystalline order at short range at 25 ºC [63]. At 25 ºC, EXAFS spectrum is characteristic to FH [60]. When the sample is treated at 300 ºC, changes in the evolution of its structure are observed as the intensity decrease of the first shell and the formation of a well-defined second shell around ~3 Å which is related to Fe-Fe interatomic distances [9]. Up to 600 ºC, EXAFS spectra do not vary significantly. Following the vertical guide of the second layer, it can be observed that it loses its symmetrical character at 700 ºC and coincides with a high presence of γ-$Fe_2O_3$ (Figs. 2 and 7). Subsequently, a large increase short-range order is observed until reaching its maximum at 900 °C, coinciding with the appearance of the ε-$Fe_2O_3$ polymorph (Figs. 3, 5, and 7). Importantly, the structural properties remain practically unchanged from 960 to 1100 ºC and the EXAFS spectra are mainly related to the ε-$Fe_2O_3$ polymorph [21]. Finally, the most abrupt structural changes are observed at 1200 ºC and they are mainly attributed to the dominant presence of α-$Fe_2O_3$ as previously has been discussed [62].

To evaluate and correlate the compositional and structural characteristics with the evolution of the magnetic properties as a function of temperature, the values of coercivity and saturation magnetization are summarized in Fig. 9. They follow similar trends and they reach their maxima values at 1040 ºC (16 emu/g and 1.6 kOe respectively). However, the saturation magnetization starts to rise from 700 ºC with the significant contribution of γ-$Fe_2O_3$ (Figs. 2d-e and 7) and the coercivity starts to grow at 900 ºC with the emergence of the ε-$Fe_2O_3$ polymorph (Figs. 3d-e and 7). At temperatures below 700 °C, both coercivity and saturation magnetization values are very low because FH is paramagnetic at room temperature and γ-$Fe_2O_3$, with sizes below 6 nm, exhibits superparamagnetism (Table 1 in the Supporting Information). On the other hand, the origin of the low coercivity of 300 Oe that is present in the 600 ºC sample is unclear (Fig. 9b). At this temperature there is a high degree of phase mixing and the FH could act as a domain wall pinning for γ-$Fe_2O_3$, as happens with other materials [64–66]. Except for this temperature, both coercivity and saturation magnetization gradually increase until 1040 °C. Above that temperature, α-$Fe_2O_3$ formation occurs more noticeably as the temperature goes up and it causes a drastic drop of the two magnitudes (Fig. 9b). When 1200 ºC is reached, α-$Fe_2O_3$ is observed as a major component of the sample and the present magnetic contribution of low coercivity and low saturation magnetization is associated with it.

Further analyses are addressed from the individual critical coercive fields (Fig. 9c), coming from the low coercivity population ($Hmax_1$) and the high coercivity population ($Hmax_2$) present in the samples. The individual coercivities of the different phases present in the sample can be guessed from the maxima in the first derivative of the hysteresis loops (not shown here). A maximum in the first derivative represents a sudden inversion of magnetization of a specific contribution of the whole sample. It is interesting to note the trend of the $Hmax_2$ in Fig. 9c, which is associated with ε-$Fe_2O_3$ nanoparticles with sizes above ~20 nm [6]. Specifically, a drastic increase is identified from 800 ºC until reaching the value of ~20 kOe at 1040 and 1100 ºC, maximum coercivity for this polymorph [6]. At 1200 ºC, $Hmax_2$ drops to virtually zero, indicating the absence of the high coercivity contribution. In turn, the magnetic contribution to the $H_{max1}$ coercivity might assigned to a residual maghemite presence below the detection limits of XRD and CRM techniques due to its high saturation magnetization (60–80 emu/g [45], to ε-$Fe_2O_3$ nanoparticles with sizes of a few nanometers [6], or to other magnetic minority phase [30]. Therefore, the compositional variations of the different compounds based on iron oxides identified by Raman experiments and semi-quantified by XAS (XANES and EXAFS) analyses (Fig. 9a), match well with their corresponding magnetic properties and this approach is proposed as a good method for calculating the compositional percentage obtained by the densification influences.

## 4. Conclusions

We have been able to correlate the occurrence of different iron-oxide phases and their magnetic properties as well as their evolution during the densification process. We have obtained coatings of iron oxide-based nanoparticles embedded in silica on commercial Si(100) substrates following an one-pot sol-gel recipe, employing GLY as a steric agent. GLY, as a reduced organic compound, greatly facilitates the formation of ε-$Fe_2O_3$ nanoparticles. The Raman properties, XANES and EXAFS analyses, and magnetic features as a function of densification temperature converge fairly well. The thermal limits are established where the iron oxide precursor micelles structurally transit through different compounds. FH is found up to 800 ºC, γ-$Fe_2O_3$ up to 900 ºC, ε-$Fe_2O_3$ between 900 and 1100 ºC, and α-$Fe_2O_3$ from 1040 to 1200 ºC. The correlation between structural and magnetic results satisfactorily elucidate the nature and properties of the compounds, identifying the highest values of saturation magnetization and coercivity for samples densified at 1040 and 1100 ºC. CRM and XAS are proposed as powerful techniques to study the evolution of ε-$Fe_2O_3$ nanoparticles which has an immense potential for multidisciplinary technological applications.

## Funding Sources

This work has been supported by the Ministerio de Ciencia e Innovación (MCINN, Spain) through the projects PIE: 2021-60-E-030, PIE: 2010-6-OE-013, PID2019-104717RB-I00 (2020–2022), MAT2017-86540-C4-1-R, RTI2018-095856-B-C21 (2019–2021), RTI2018-097895-B-C43 and RTI2018-095303-A-C52. The authors are grateful to The ESRF (France), MCINN and Consejo Superior de Investigations Científicas (CSIC, Spain) for the provision of synchrotron radiation facilities and to the BM25-SpLine Staff for their valuable help. A.S. and A.M.-N acknowledge financial support from Comunidad de Madrid (Spain) for an "Atracción de Talento Investigador" Contract 2017-t2/IND5395 and 2018-T1/IND-10360, respectively.

## CRediT authorship contribution statement

J. L.-S., O. R. d. l. F. and N. C. conceived the work and coordinated the research. J. L.-S. prepared the samples. A. d. C. carried out the confocal Raman experiment. A. S., E. S.-C., A. M.-N., G. R. C., J. L.-S. M. A., M. C., M. V. and J. R.-Z carried out the structural characterization. J. L.-S. performed the magnetic characterization. All authors wrote and revised the manuscript and extensively discussed the results and their interpretation.

## Declaration of Competing Interest

The authors declare that they have no known competing financial interests or personal relationships that could have appeared to influence the work reported in this paper.

## Appendix A. Supporting information

Supplementary data associated with this article can be found in the online version at doi:10.1016/j.jallcom.2021.162061.

## References

[1] J. Jin, S. Ohkoshi, K. Hashimoto, Giant coercive field of nanometer-sized iron oxide, Adv. Mater. 16 (2004) 48–51, https://doi.org/10.1002/adma.200305297
[2] M. Popovici, M. Gich, D. Nižňanský, A. Roig, C. Savii, L. Casas, E. Molins, K. Zaveta, C. Enache, J. Sort, S. De Brion, G. Chouteau, J. Nogués, Optimized synthesis of the elusive ε-$Fe_2O_3$ phase via sol-gel chemistry, Chem. Mater. 16 (2004) 5542–5548, https://doi.org/10.1021/cm048628m
[3] M. Tadic, I. Milosevic, S. Kralj, D. Hanzel, T. Barudzija, L. Motte, D. Makovec, Surface-induced reversal of a phase transformation for the synthesis of ε-$Fe_2O_3$ nanoparticles with high coercivity, Acta Mater. 188 (2020) 16–22, https://doi.org/10.1016/j.actamat.2020.01.058
[4] J.L. García-Muñoz, A. Romaguera, F. Fauth, J. Nogues, M. Gich, Unveiling a new high-temperature ordered magnetic phase in ε-$Fe_2O_3$, Chem. Mater. 29 (2017) 9705–9713, https://doi.org/10.1021/acs.chemmater.7b03417
[5] M. Gich, C. Frontera, A. Roig, E. Taboada, E. Molins, H.R. Rechenberg, J.D. Ardisson, W.A.A. Macedo, C. Ritter, V. Hardy, J. Sort, V. Skumryev, J. Nogues, High- and low-temperature crystal and magnetic structures of ε-$Fe_2O_3$ and their correlation to its magnetic properties, Chem. Mater. 3 (2006) 3889–3897, https://doi.org/10.1021/cm060993l
[6] S. Ohkoshi, A. Namai, K. Imoto, M. Yoshikiyo, W. Tarora, K. Nakagawa, M. Komine, Y. Miyamoto, T. Nasu, S. Oka, H. Tokoro, Nanometer-size hard magnetic ferrite exhibiting high optical-transparency and nonlinear optical-magnetoelectric effect, Sci. Rep. 5 (2015) 14414, https://doi.org/10.1038/srep14414
[7] M. Tadic, V. Spasojević, V. Kusigerski, D. Marković, M. Remškar, Formation of ε-$Fe_2O_3$ phase by the heat treatment of α-$Fe_2O_3$/$SiO_2$ nanocomposite, Scr. Mater. 58 (2008) 703–706, https://doi.org/10.1016/j.scriptamat.2007.12.009
[8] V.N. Nikolic, M. Tadić, M. Panjan, L. Kopanja, N. Cvjetićanin, V. Spasojević, Influence of annealing treatment on magnetic properties of $Fe_2O_3$/$SiO_2$ and formation of ε-$Fe_2O_3$ phase, Ceram. Int. 43 (2017) 3147–3155, https://doi.org/10.1016/j.ceramint.2016.11.132
[9] J. López-Sánchez, A. Serrano, A. del Campo, M. Abuín, E. Salas-Colera, A. Muñoz-Noval, G.R. Castro, J. de la Figuera, J.F. Marco, P. Marín, N. Carmona, O. Rodríguez de la Fuente, Self-assembly of iron oxide precursor micelles driven by magnetic stirring time in sol–gel coatings, RSC Adv. 9 (2019) 17571–17580, https://doi.org/10.1039/C9RA03283E
[10] V.N. Nikolic, V. Spasojevic, M. Panjan, L. Kopanja, A. Mrakovic, M. Tadic, Re-formation of metastable ε-$Fe_2O_3$ in post-annealing of $Fe_2O3$/$SiO_2$nanostructure: synthesis, computational particle shape analysis in micrographs and magnetic properties, Ceram. Int. 43 (2017) 7497–7507, https://doi.org/10.1016/j.ceramint.2017.03.030
[11] M. Gich, I. Fina, A. Morelli, F. Sánchez, M. Alexe, J. Gàzquez, J. Fontcuberta, A. Roig, Multiferroic iron oxide thin films at room temperature, Adv. Mater. 26 (2014) 4645–4652, https://doi.org/10.1002/adma.201400990
[12] V. Ukleev, M. Volkov, A. Korovin, T. Saerbeck, N. Sokolov, S. Suturin, Stabilization of ε-$Fe_2O_3$ epitaxial layer on MgO(111)/GaN via an intermediate γ-phase, Phys. Rev. Mater. 3 (2019) 25–28, https://doi.org/10.1103/PhysRevMaterials.3.094401
[13] M. Gich, J. Gazquez, A. Roig, A. Crespi, J. Fontcuberta, J.C. Idrobo, S.J. Pennycook, M. Varela, V. Skumryev, M. Varela, Epitaxial stabilization of ε-$Fe_2O_3$ (00l) thin films on $SrTiO_3$ (111), Appl. Phys. Lett. 96 (2010) 2008–2011, https://doi.org/10.1063/1.3360217
[14] T.M.N. Thai, D.T. Nguyen, N.-S. Lee, J.-S. Rhyee, J. Song, H.-J. Kim, Stabilization of metastable ε-$Fe_2O_3$ thin films using a $GaFeO_3$ buffer, J. Appl. Phys. 120 (2016) 185304, https://doi.org/10.1063/1.4967393
[15] A. Philip, J.P. Niemelä, G.C. Tewari, B. Putz, T.E.J. Edwards, M. Itoh, I. Utke, M. Karppinen, Flexible ε-$Fe_2O_3$-terephthalate thin-film magnets through ALD/MLD, ACS Appl. Mater. Interfaces 12 (2020) 21912–21921, https://doi.org/10.1021/acsami.0c04665
[16] L. MacHala, J. Tuček, R. Zbořil, Polymorphous transformations of nanometric iron (III) oxide: a review, Chem. Mater. 23 (2011) 3255–3272, https://doi.org/10.1021/cm200397g
[17] K. Kelm, W. Mader, Synthesis and structural analysis of ε-$Fe_2O_3$, Z. Fur Anorg. Und Allg. Chem. 631 (2005) 2383–2389, https://doi.org/10.1002/zaac.200500283
[18] C. Kadlec, F. Kadlec, V. Goian, M. Gich, M. Kempa, S. Rols, M. Savinov, J. Prokleška, M. Orlita, S. Kamba, Electromagnon in ferrimagnetic ε-$Fe_2O_3$ nanograin ceramics, Phys. Rev. B Condens. Matter Mater. Phys. 88 (2013) 1–8, https://doi.org/10.1103/PhysRevB.88.104301
[19] M. Gich, C. Frontera, A. Roig, E. Molins, J. Fontcuberta, N. Bellido, C. Simon, C. Fleta, Magnetoelectric coupling in epsilon-$Fe_2O_3$ nanoparticles, Nanotechnology 17 (2006) 687–691, https://doi.org/10.1088/0957-4484/17/3/012
[20] J.A. Sans, V. Monteseguro, G. Garbarino, M. Gich, T. Irifune, A. Muñoz, C. Popescu, V. Cerantola, V. Cuartero, M. Monte, Stability and nature of the volume collapse of ε-$Fe_2O_3$ under extreme conditions, Nat. Commun. 9 (2018) 1–11, https://doi.org/10.1038/s41467-018-06966-9
[21] J. López-Sánchez, A. Muñoz-Noval, C. Castellano, A. Serrano, A. del Campo, M. Cabero, M. Varela, M. Abuín, J. de la Figuera, J.F. Marco, G.R. Castro, O. Rodriguez de la Fuente, N. Carmona, Origin of the magnetic transition at 100 K in ε-$Fe_2O_3$ nanoparticles studied by X-ray absorption fine structure spectroscopy, J. Phys. Condens. Matter 29 (2017) 485701, https://doi.org/10.1088/1361-648X/aa904b
[22] S.I. Ohkoshi, M. Yoshikiyo, Y. Umeta, M. Komine, R. Fujiwara, H. Tokoro, K. Chiba, T. Soejima, A. Namai, Y. Miyamoto, T. Nasu, Phonon-mode calculation, far- and mid-infrared, and raman spectra of an ε-$Ga_{0.5}Fe_{1.5}O_3$ magnet, J. Phys. Chem. C 121 (2017) 5812–5819, https://doi.org/10.1021/acs.jpcc.6b12694
[23] J. López-Sánchez, A. Serrano, A. Del Campo, M. Abuín, O. Rodríguez de la Fuente, N. Carmona, Sol–gel synthesis and micro-raman characterization of ε-$Fe_2O_3$ micro- and nanoparticles, Chem. Mater. 28 (2016) 511–518, https://doi.org/10.1021/acs.chemmater.5b03566
[24] A. Namai, S. Ohkoshi, High-frequency millimeter wave absorber composed of a new series of iron oxide nanomagnets, in: M. Khatib (Ed.), Adv. Trends Wirel. Commun. InTech, 2011, pp. 493–504, https://doi.org/10.5772/655
[25] Y. Gu, M. Yoshikiyo, A. Namai, D. Bonvin, A. Martinez, R. Piñol, P. Téllez, N.J.O. Silva, F. Ahrentorp, C. Johansson, J. Marco-Brualla, R. Moreno-Loshuertos, P. Fernández-Silva, Y. Cui, S.I. Ohkoshi, A. Millán, Magnetic hyperthermia with ε-$Fe_2O_3$ nanoparticles, RSC Adv. 10 (2020) 28786–28797, https://doi.org/10.1039/d0ra04361c
[26] S.I. Ohkoshi, K. Imoto, A. Namai, M. Yoshikiyo, S. Miyashita, H. Qiu, S. Kimoto, K. Kato, M. Nakajima, Rapid Faraday rotation on ε-iron oxide magnetic nanoparticles by visible and terahertz pulsed light, J. Am. Chem. Soc. 141 (2019) 1775–1780, https://doi.org/10.1021/jacs.8b12910
[27] A. Namai, S. Kurahashi, T. Goto, S.I. Ohkoshi, Theoretical design of a high-frequency millimeter wave absorbing sheet composed of gallium substituted ε-$Fe_2O_3$ nanomagnet, IEEE Trans. Magn. 48 (2012) 4386–4389, https://doi.org/10.1109/TMAG.2012.2199091
[28] S. Ohkoshi, S. Kuroki, S. Sakurai, K. Matsumoto, K. Sato, S. Sasaki, A new millimeter wave absorber based on gallium-substituted ε-iron oxide nanomagnets, Angew. Chem. Int. Ed. 13 (2007) 195–206, https://doi.org/10.1177/1460458207079900
[29] J. López-Sánchez, G. McIntosh, M.L. Osete, A. del Campo, J.J. Villalaín, L. Pérez, M. Kovacheva, O. Rodríguez de la Fuente, Epsilon iron oxide: origin of the high coercivity stable low Curie temperature magnetic phase found in heated archeological materials, Geochem. Geophys. Geosyst. 18 (2017) 2646–2656, https://doi.org/10.1002/2017GC006929
[30] J. López-Sánchez, A. Palencia-Ortas, A. del Campo, G. McIntosh, M. Kovacheva, F. Martín-Hernández, N. Carmona, O. Rodríguez de la Fuente, P. Marín, A. Molina-Cardín, M.L. Osete, Further progress in the study of epsilon iron oxide in archaeological baked clays, Phys. Earth Planet. Inter. 307 (2020) 106554, https://doi.org/10.1016/j.pepi.2020.106554
[31] H. Tokoro, A. Namai, S.I. Ohkoshi, Advances in magnetic films of epsilon-iron oxide toward next-generation high-density recording media, Dalt. Trans. 50 (2021) 452–459, https://doi.org/10.1039/d0dt03460f
[32] R. Zboril, M. Mashlan, D. Petridis, Iron(III) oxides from thermal processes-synthesis, structural and magnetic properties, Mössbauer spectroscopy

characterization, and applications, Chem. Mater. 14 (2002) 969–982, https://doi.org/10.1021/cm0111074
[33] J. López-Sánchez, A. Muñoz-Noval, A. Serrano, M. Abuín, J. de la Figuera, J.F. Marco, L. Perez, N. Carmona, O. Rodríguez de la Fuente, Growth, structure and magnetism of ε-$Fe_2O_3$ in nanoparticle form, RSC Adv. 6 (2016) 46380–46387, https://doi.org/10.1039/C6RA01912A
[34] C.E. Kim, J.S. Yoon, H.J. Hwang, Synthesis of nanoporous silica aerogel by ambient pressure drying, J. Sol. Gel Sci. Technol. 49 (2009) 47–52, https://doi.org/10.1007/s10971-008-1828-7
[35] A.V. Rao, M.M. Kulkarni, Effect of glycerol additive on physical properties of hydrophobic silica aerogels, Mater. Chem. Phys. 77 (2002) 819–825, https://doi.org/10.1016/S0254-0584(02)00207-9
[36] J. Kohout, P. Brázda, K. Závěta, D. Kubániová, T. Kmječ, L. Kubíčková, M. Klementová, E. Šantavá, A. Lančok, The magnetic transition in ε-$Fe_2O_3$ nanoparticles: magnetic properties and hyperfine interactions from Mössbauer spectroscopy, J. Appl. Phys. 117 (2015) 2–6, https://doi.org/10.1063/1.4907610
[37] A. Serrano, Modified Au-Based Nanomaterials Studied by Surface Plasmon Resonance Spectroscopy, Springer, 2015, https://doi.org/10.1007/978-3-319-19402-8
[38] B. Ravel, M. Newville, ATHENA, ARTEMIS, HEPHAESTUS: Data analysis for X-ray absorption spectroscopy using IFEFFIT, J. Synchrotron Radiat. 12 (2005) 537–541, https://doi.org/10.1107/S0909049505012719
[39] L. Bellot-Gurlet, D. Neff, S. Réguer, J. Monnier, M. Saheb, P. Dillmann, Raman studies of corrosion layers formed on archaeological irons in various media, J. Nano Res. 8 (2009) 147–156, https://doi.org/10.4028/www.scientific.net/JNanoR.8.147
[40] K. Uchinokura, T. Sekine, E. Matsuura, Raman scattering by silicon, Solid State Commun. 11 (1972) 47–49, https://doi.org/10.1016/0038-1098(72)91127-1
[41] D.L.A. de Faria, S. Venancio Silva, M.T. de Oliveira, Raman microspectroscopy of some iron oxides and oxyhydroxides, J. Raman Spectrosc. 28 (1997) 873–878, https://doi.org/10.1002/(SICI)1097-4555(199711)28:11<873::AID-JRS177>3.0.CO;2-B
[42] A.M. Jubb, H.C. Allen, Vibrational spectroscopic characterization of hematite, maghemite, and magnetite thin films produced by vapor deposition, ACS Appl. Mater. Interfaces 2 (2010) 2804–2812, https://doi.org/10.1021/am1004943
[43] X. Wang, M. Zhu, L.K. Koopal, W. Li, W. Xu, F. Liu, J. Zhang, Q. Liu, X. Feng, D.L. Sparks, Effects of crystallite size on the structure and magnetism of ferrihydrite, Environ. Sci. Nano 3 (2016) 190–202, https://doi.org/10.1039/C5EN00191A
[44] Y. Guyodo, S.K. Banerjee, R. Lee Penn, D. Burleson, T.S. Berquo, T. Seda, P. Solheid, Magnetic properties of synthetic six-line ferrihydrite nanoparticles, Phys. Earth Planet. Inter. 154 (2006) 222–233, https://doi.org/10.1016/j.pepi.2005.05.009
[45] R.M. Cornell, U. Schwertmann, The Iron Oxides, Wiley, Weinheim; Germany, 2003, https://doi.org/10.1002/3527602097
[46] T.S. Berquó, S.K. Banerjee, R.G. Ford, R.L. Penn, T. Pichler, High crystallinity Si-ferrihydrite: an insight into its Néel temperature and size dependence of magnetic properties, J. Geophys. Res. Solid Earth. 112 (2007) 1–12, https://doi.org/10.1029/2006JB004583
[47] J.G.E. Harris, J.E. Grimaldi, D.D. Awschalom, A. Chiolero, D. Loss, Excess spin and the dynamics of antiferromagnetic ferritin, Phys. Rev. B 60 (1999) 3453–3456, https://doi.org/10.1103/PhysRevB.60.3453
[48] M.F. Hochella, S.K. Lower, P.A. Maurice, R.L. Penn, N. Sahai, D.L. Sparks, B.S. Twining, Nanominerals, mineral nanoparticles, and earth systems, Science 319 (2008) 1631–1635, https://doi.org/10.1126/science.1141134
[49] C.J. Masina, J.H. Neethling, E.J. Olivier, S. Manzini, L. Lodya, V. Srot, P.A. van Aken, Structural and magnetic properties of ferrihydrite nanoparticles, RSC Adv. 5 (2015) 39643–39650, https://doi.org/10.1039/C5RA06936J
[50] Q.A. Pankhurst, J. Connolly, S.K. Jones, Applications of magnetic nanoparticles in biomedicine, J. Phys. D Appl. Phys. 36 (2003) R167–R181, https://doi.org/10.1088/0022-3727/36/13/201
[51] L. Néel, Theorie du trainage magnetique des ferromagnetiques en grains fins avec applications aux terres cuites, Ann. Geophys. 5 (1949) 99–136, https://doi.org/10.1017/CBO9781107415324.004
[52] L.A. Mercante, W.W.M. Melo, M. Granada, H.E. Troiani, W.A.A. MacEdo, J.D. Ardison, M.G.F. Vaz, M.A. Novak, Magnetic properties of nanoscale crystalline maghemite obtained by a new synthetic route, J. Magn. Magn. Mater. 324 (2012) 3029–3033, https://doi.org/10.1016/j.jmmm.2012.04.049
[53] M. Gich, A. Roig, C. Frontera, E. Molins, J. Sort, M. Popovici, G. Chouteau, D. Martín, y Marero, J. Nogués, Large coercivity and low-temperature magnetic reorientation in ε-$Fe_2O_3$ nanoparticles, J. Appl. Phys. 98 (2005) 044307, https://doi.org/10.1063/1.1997297
[54] O.N. Shebanova, P. Lazor, Raman spectroscopic study of magnetite ($FeFe_2O_4$): a new assignment for the vibrational spectrum, J. Solid State Chem. 174 (2003) 424–430, https://doi.org/10.1016/S0022-4596(03)00294-9
[55] D.H. Pearson, C.C. Ahn, B. Fultz, White lines and d-electron occupancies for the 3d and 4d transition metals, Phys. Rev. B 47 (1993) 8471–8478, https://doi.org/10.1103/PhysRevB.47.8471
[56] Haiyan Tan, J. Verbeeck, A. Abakumov, V.T. Gustaaf, Oxidation state and chemical shift investigation in transition metal oxides by EELS, Ultramicroscopy 116 (2012) 24–33.
[57] A. Longo, X.L. Wang, A. Ruotolo, A. Peluso, G. Carotenuto, R. Lortz, Effect of the polymeric matrix on the structural and magnetic properties of hematite/polymer composites, J. Nanopart. Res. 14 (2012) 1314, https://doi.org/10.1007/s11051-012-1314-6
[58] L. Del Bianco, D. Fiorani, A.M. Testa, E. Bonetti, L. Savini, S. Signoretti, Magnetothermal behavior of a nanoscale Fe/Fe oxide granular system, Phys. Rev. B 66 (2002) 174418, https://doi.org/10.1103/PhysRevB.66.174418
[59] M. Fracchia, M. Manzoli, U. Anselmi-Tamburini, P. Ghigna, A new eight-cation inverse high entropy spinel with large configurational entropy in both tetrahedral and octahedral sites: Synthesis and cation distribution by X-ray absorption spectroscopy, Scr. Mater. 188 (2020) 26–31, https://doi.org/10.1016/j.scriptamat.2020.07.002
[60] A. Corrias, G. Ennas, G. Mountjoy, G. Paschina, An X-ray absorption spectroscopy study of the FeK edge in nanosized maghemite and in $Fe_2O_3$-$SiO_2$ nanocomposites, Phys. Chem. Chem. Phys. 2 (2010) 1045–1050 ⟨http://kar.kent.ac.uk/16325/⟩.
[61] W.A. Hendrickson, M.S. Co, J.L. Smith, K.O. Hodgson, G.L. Klippenstein, X-ray absorption spectroscopy of the dimeric iron site in azidomethemerythrin from Phascolopsis gouldii, Proc. Natl. Acad. Sci. USA 79 (1982) 6255–6259, https://doi.org/10.1073/pnas.79.20.6255
[62] A. Serrano, J. Rubio-Zuazo, J. López-Sánchez, E. Enríquez, E. Salas-Cólera, G.R. Castro, Nanostructured Au(111)/oxide epitaxial heterostructures with tailoring plasmonic response by a one-step strategy, J. Phys. Chem. C 123 (2019) 25294–25302, https://doi.org/10.1021/acs.jpcc.9b04768
[63] A.N. Kravtsova, Synchrotron-based X-ray absorption spectroscopy for the study of geological materials, J. Surf. Investig. X Ray Synchrotron Neutron Tech. 14 (2020) 135–149, https://doi.org/10.1134/S1027451020020111
[64] P.G.B. Gueye, J. López-Sánchez, E. Navarro, A. Serrano, P. Marín, Control of the length of $Fe_{73.5}Si_{13.5}Nb_3Cu_1B_9$ microwires to be used for magnetic and microwave absorbing purposes, ACS Appl. Mater. Interfaces 12 (2020) 15644–15656, https://doi.org/10.1021/acsami.9b21865
[65] J. López Sánchez, E. Navarro, A. Serrano, C. Granados-Miralles, A. Del Campo, A. Quesada, P. Marín, Ultrafast particle size reduction of $Fe_{73.9}Si_{15.5}Cu_1Nb_3B_{6.6}$ by high-energy milling: $Nb_2O_5$ as a marker of permeability enhancement and magnetic hardening, ACS Appl. Electron. Mater. 2 (2020) 1484–1496, https://doi.org/10.1021/acsaelm.0c00252
[66] J. López-Sánchez, E. Navarro, F. Rodríguez-Granado, A. Serrano, P. Marín, Multiphase materials based on the $Fe_{73.9}Si_{15.5}Cu_1Nb_3B_{6.6}$ alloy obtained by dry and wet high-energy ball milling processes, J. Alloys Compd. 864 (2021) 158136, https://doi.org/10.1016/j.jallcom.2020.158136